

Beyond Core and Penumbra: Bi-Temporal Image-Driven Stroke Evolution Analysis

Md Sazidur Rahman¹

MD.S.RAHMAN@UIS.NO

Kjersti Engan¹

KJERSTI.ENGAN@UIS.NO

Kathinka Dæhli Kurz^{1,2}

KATHINKA.DEHLI.KURZ@SUS.NO

Mahdieh Khanmohammadi¹

MAHDIEH.KHANMOHAMMADI@UIS.NO

¹ Department of Electrical Engineering and Computer Science, University of Stavanger, Norway

² Stavanger Medical Imaging Laboratory, Stavanger University, Hospital, Norway

Abstract

Computed tomography perfusion (CTP) at admission is routinely used to estimate hypoperfused brain region comprising damaged tissue (ischemic core) and its surrounding tissue at risk (penumbra), whereas follow-up diffusion-weighted MRI (DWI) obtained after treatment provides the definitive infarct outcome. However, single time-point segmentations do not capture the biological heterogeneity of stroke and ignore its continuous temporal evolution. In this work we explore the differences in hypoperfused areas that end up being either infarcted or re-perfused and can be seen as tissue characterization. We propose a bi-temporal analysis framework that characterizes ischemic tissue using statistical descriptors, radiomic texture features, and deep feature embeddings from two architectures (mJ-Net and nnU-Net). Bi-temporal refers to the admission (T_1) and the first post-treatment follow-up (T_2). All features are extracted at T_1 from CTP, and follow-up DWI is aligned with CTP to ensure spatial correspondence. Manually delineated masks at T_1 and T_2 are intersected to construct six regions of interest encoding both initial tissue state and final outcome. Extracted features were aggregated per region and analyzed in feature space. Evaluation on 18 patients with successful reperfusion demonstrated meaningful clustering of region-level representations. Regions classified as penumbra or healthy at T_1 that ultimately recovered exhibited feature similarity to preserved brain tissue, whereas infarct-bound regions formed distinct groupings.

Both baseline, GLCM deep embeddings showed a similar trend: penumbra regions show features that are significantly different depending on final state, whereas this difference is not significant for core regions. Deep feature spaces, particularly mJ-Net, showed strong separation between salvageable and non-salvageable tissue, with a penumbra separation index that differed significantly from zero (Wilcoxon signed-rank test: $p = 1.5 \times 10^{-5}$). These findings suggest that encoder-derived feature manifolds may reflect underlying tissue phenotypes and state transitions, providing an insight into imaging-based quantification of stroke evolution.

Keywords: Perfusion imaging, CTP, Diffusion MRI, DWI, Radiomic features, CNN embedding, Stroke progression analysis.

1. Introduction

Computed tomography perfusion (CTP) is widely used at the hyper-acute stage at hospital admission, referred to as T_1 in this paper, to quantify cerebral hemodynamics and estimate hypoperfused brain volumes including highly likely damaged tissue called ischemic

core and salvageable surrounding tissue called penumbra. Ischemia is not clearly visible in raw CTP. However, from time-attenuation curves, perfusion parametric maps are derived to enable rapid assessment of tissue viability. The parametric maps include cerebral blood flow (CBF), cerebral blood volume (CBV), mean transit time (MTT), time to peak (TTP), and time-to-maximum (Tmax) (Wintermark et al., 2006). Using parametric maps, severely hypoperfused regions are typically classified as ischemic core, whereas moderately hypoperfused regions represent penumbra, tissue that may still be salvageable with timely reperfusion.

Magnetic resonance diffusion-weighted imaging (DWI) is highly sensitive to irreversible cellular injury and is considered the definitive marker of infarcted brain tissue (Yang et al., 2022). Although DWI visualizes ischemia more clearly than CT, its longer acquisition time means it is typically obtained 24-72 hours post-stroke at the first follow-up time point (T_2). These images reveal the eventual infarct outcome, serving as ground truth for which threatened tissue ultimately died or survived (Yang et al., 2022). Current stroke guidelines allow treatment in selected patients up to 24 hours after onset (Mainali et al., 2021). In practice, patients with small infarct cores and large regions of hypoperfused but salvageable tissue can benefit from reperfusion therapies well beyond the traditional time window of 4.5 or 6 hours (Mainali et al., 2021; Werdiger et al., 2023; Nogueira et al., 2018).

Segmentation approaches on CTP and DWI provide operational definitions of core, penumbra and final infarct regions. Yet these methods often fail to capture the full biological heterogeneity, temporal dynamics of ischemic tissue injury, and how it evolves with treatment (Werdiger et al., 2023). Radiomics and advanced feature extraction methods are rapidly evolving in stroke neuroimaging, with work spanning technical foundations and modality-specific clinical applications. Jiang et al. (Jiang et al., 2023) combined DWI radiomic features with clinical variables to predict unfavorable long-term outcomes after acute ischemic stroke, showing how DWI-derived radiomic signatures can strengthen prognostic models beyond conventional imaging. Research outside ischemic stroke, such as Tran et al. (Tran et al., 2025), comparing handcrafted radiomics with latent deep features from admission head CT in intracerebral hemorrhage, similarly found that deep features modestly outperform classical radiomics—highlighting a broader trend in feature extraction that is likely relevant for stroke imaging as well.

Imaging phenotyping involves extracting and defining meaningful patterns or subtypes from imaging data that reflect underlying tissue physiology or disease states (Van Timmeren et al., 2020). Population-scale imaging studies show that automated lesion segmentation yields robust imaging phenotypes (e.g., lesion volume and topography) that stratify patients and reflect stroke subtypes, highlighting the value of standardized quantitative descriptors over ad-hoc assessments (Wu et al., 2019). Trajectory-based analyses reveal that recovery patterns cluster into distinct, predictable subtypes, indicating that stroke phenotypes are dynamic processes rather than single time-point observations (Krishnagopal et al., 2022). The phenotyping in ischemic stroke means defining tissue-state subtypes that are not only relying on a single stroke time point but rather be defined using bi-temporal imaging signatures. It links stroke lesions admission-time perfusion characteristics to follow-up diffusion outcome lesion.

Recent advances in deep learning have significantly improved the estimation of ischemic core and penumbra from CTP (Tomasetti et al., 2022a,b). Instead of relying solely on

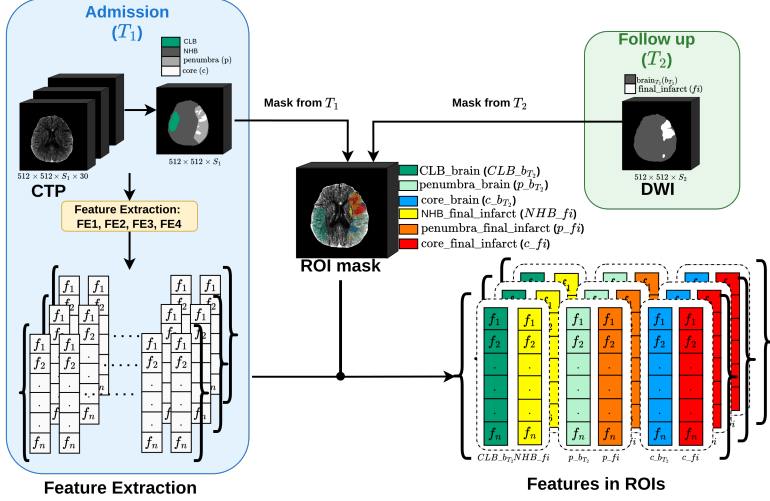


Figure 1: Framework of the proposed method. Acute ischemic regions from CTP at T_1 are combined with final tissue outcome from DWI at T_2 to form six ROI classes. Image-derived features from four extraction methods are computed on CTP and grouped according to ROI membership.

derived perfusion maps, modern architectures leverage spatiotemporal CTP data to learn representations that more accurately segment at-risk tissue (Tomasetti et al., 2023). However, while deep learning enables high performance, the learned latent features that drive segmentation accuracy remain underexplored.

In this study, we aim to investigate differences within hypoperfused brain tissue at the time of admission (T_1) that subsequently evolves into either infarcted tissue or reperfused (salvaged) tissue at follow-up (T_2). This analysis can be regarded as a form of tissue characterization. Specifically, we examine imaging-derived features that describe ischemic regions and assess their potential to predict tissue outcome and salvageability. We propose a framework, shown in figure 1, for quantitative bi-temporal analysis of ischemic tissue evolution. At admission (T_1), core, penumbra, and healthy regions are characterized using image-driven signatures comprising statistical descriptors, radiomic texture features, and deep convolutional neural network (CNN) embeddings. Deep representations are derived from two segmentation architectures, a 2D+time mJNet model (Tomasetti et al., 2020) and a 2D nnU-Net framework (Isensee et al., 2021), whose internal feature maps may provide multi-level descriptors of tissue state beyond segmentation outputs. These admission-time signatures are then tracked to follow-up imaging to determine which regions recover and which progress to infarction. Multiple region of interest (ROI) are constructed by combining manually labeled regions in CTP taken at T_1 and in DWI obtained at T_2 .

We hypothesize that the progression of ischemic tissue and its outcome can be described as tissue phenotyping or clustering patterns in feature space, where each coordinate represents a feature encoding intensity, texture, or latent CNN representation.

2. Dataset Description

The data was acquired at Stavanger University Hospital at two different time points: at admission (T_1) full CT protocol including non-contrast CT (NCCT), CT angiography and CT perfusion scans are obtained. Then after treatment at the first follow up (T_2) usually (24 to 72) hours later, magnetic resonance imaging (MRI) protocol is run and diffusion weighted images (DWI), are obtained. In this paper we use CTP from T_1 and DWI from T_2 . CTP studies are acquired over a slab of the brain during the first pass of iodinated contrast (Omnipaque 350mg/ml) followed by isotonic saline (total 80ml; 6ml/s, 4s delay). Each study comprises 512×512 images of 13-22 brain slices of resolution $0.425 \times 0.425 \times 5$ mm and a temporal sampling of 30 time points, the first 20 sampled with 1 sec interval, the last 10 at 2 sec. DWI scans are obtained as 3D volumes with typically 24–60 brain slices in the axial axis and in-plane resolution between (176×176) and (384×384) .

The full dataset includes 152 acute ischemic stroke patients, where 109 have also gone through the MRI protocol. Among those 61 showed large vessel occlusion (LVO), where in 48 of them blood flow were preserved after treatment. We refer to them as recanalized patients in the remainder of this article. Among those 18 patients were selected for this analysis based on the availability of follow-up DWI imaging, successful spatial co-registration between CTP and DWI, and complete manual annotations of ischemic regions.

3. Preprocessing and region of interest construction

The CTP is 4-dimensional (4D) data we denote as $V_0(x, y, z, t) \in \mathbb{R}^{512 \times 512 \times S_1 \times 30}$, where x and y are the spatial coordinates (resolution 512×512), S_1 corresponds to the number of brain slices taken at T_1 , indexed by z and varies between (13-22). t is the time index ($t \in \{1 \dots 30\}$). The CTP volumes were rigidly registered to the first time point using an intensity-based similarity transform to correct for motion within the perfusion sequence. An automatic brain extraction method ([Najm et al., 2019](#)) was used for skull stripping to remove bone, scalp, and other non-brain tissues. We denote the preprocessed CTP volumes as $V(v, t)$ where we define $\Omega \subset \mathbb{Z}^3$ and $v \in \Omega$ as the volumetric index. Looking at CTP slice by slice including all time points is denote as $V(\bar{x}, z_i)$, $\bar{x} \in [x, y, t]$ for a specific slice z_i .

3.1. Region of interest construction

The registration and region of interest definitions are illustrated in figure 2.

T_1 and T_2 alignment: The DWI volume typically has lower in-plane resolution and covers a larger cranial extent than CTP. Therefore we need to register the DWI slices to the CTP brain slab. Thus, the DWI volumes $D_0(x, y, z)$ were first cropped in the z -direction to match the axial slices overlapping the CTP slab. The cropped DWI volume was then registered to the corresponding CTP using a similarity transform driven by an intensity-based similarity metric and resampled onto the CTP grid (in-plane 512×512). This procedure ensured spatial alignment between the follow-up infarct and the acute perfusion sequence. We denote the registered DWI-CTP pair as $(D(v), V(v, t))$, and for one slice $(D(\tilde{x}, z_1), V(\bar{x}, z_1))$, where \tilde{x} corresponds to $(\bar{x}$ but exclusive the time axis).

Ground-truth labels were produced by two expert neuroradiologists through manual delineation using an in-house MATLAB-based software ([Tomasetti et al., 2023, 2022b](#)). For

the T_1 time point, the full CT examination, including Non-Contrast CT, CT angiography and preprocessed CTP, and perfusion maps(CBV, CBF, TTP, and maximum intensity projection (MIP)) was used. Regions with increased TTP/Tmax and reduced CBF but preserved CBV were considered penumbra (p), whereas additional CBV reduction indicated ischemic core (c). Final infarct masks ($fi \in \Omega$) were manually delineated on DWI by an expert radiologist, and the remaining brain voxels at T_2 were labeled as $b \in \Omega$. To account for small boundary inconsistencies, the ischemic core mask ($c \in \Omega$) was morphologically dilated by a small structure element, and in our work the penumbra ($p \in \Omega$) is defined as the marked penumbra region excluding all voxels belonging to the core. To avoid perfusion-related bias, a region from the contra-lateral hemisphere of the brain at T_1 was annotated and used as healthy brain tissue, called CLB $\in \Omega$. The remaining brain tissue at T_1 is denoted Not hypo-perfused brain: NHB $\in \Omega$.

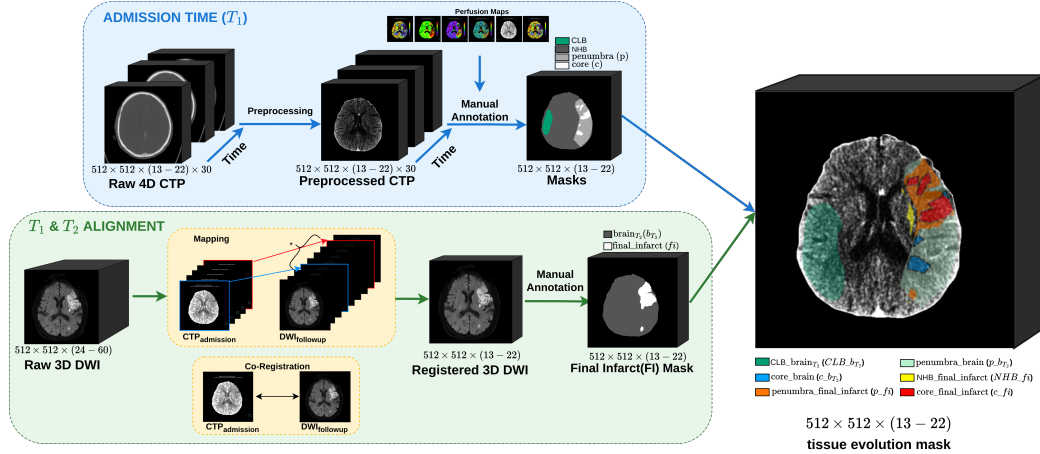


Figure 2: Construction of the tissue bi-temporal masks by combining manual delineation at admission (T_1) and follow-up (T_2). At T_1 , preprocessed 4D CTP is annotated into brain, penumbra and core. At T_2 , DWI is mapped to CTP slab and DWI co-registered to CTP is annotated for final infarct. The T_1 and T_2 masks are then merged into six-ROI mask.

Bi-temporal ROI logic: To model tissue evolution over time, defined regions at T_1 were combined with regions at T_2 through region mapping and set intersections. Formally, each voxel v was assigned to one of the following ROIs based on the rule:

$$ROI_{R_{T_1}}^{R_{T_2}} := R_{T_1} \cap R_{T_2}$$

This resulted in a categorical bi-temporal tissue evolution maps $ROI_{R_{T_1}}^{R_{T_2}} \in \Omega$ that gives the regions for our further investigations:

4. Methods

To characterize ischemic tissue, we do image feature extraction (FE) from preprocessed CTP and relate them to final outcome on follow-up DWI. We consider three feature families

ROI_{CLB}^b	healthy tissue from contralateral hemisphere at admission and remained healthy
ROI_{NHB}^b	tissue initially appearing normal (not hypo-perfused(NHB)) but later infarcted
ROI_p^b	penumbral tissue that recovered fully
ROI_p^i	penumbra that progressed to infarction
ROI_c^b	core tissue showing partial or unexpected recovery
ROI_c^i	core that remained infarcted at follow-up

baseline statistical descriptors, radiomic texture metrics, and deep CNN embeddings which together capture complementary aspects of tissue heterogeneity and provide a compact representation of stroke evolution between the two time points.

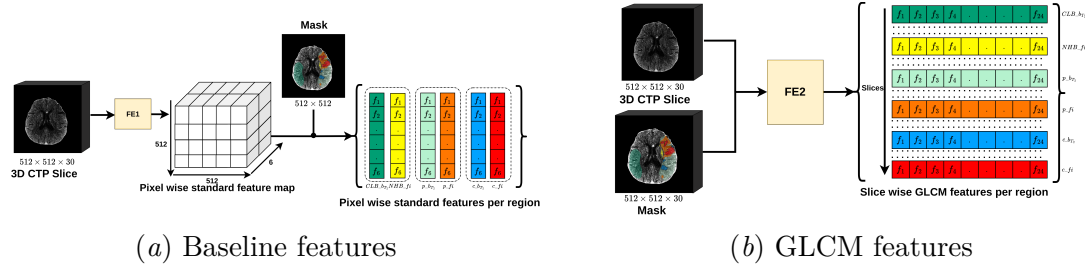


Figure 3: Baseline and GLCM feature extraction. (a) Baseline features are computed using a $3 \times 3 \times 30$ sliding window on CTP and aggregated into region-wise vectors via tissue evolution masks. (b) Radiomic-based 3D GLCM features are extracted per slice and assigned to each tissue evolution class.

(FE1) Baseline (BL) statistical features are directly derived from 3D CTP data $V(\bar{x}, z_i)$. To extract the features, we use a sliding window $\mathcal{W}(\bar{x}) \in \mathbb{R}^{3 \times 3 \times 30}$ centered around \bar{x} . From the intensities in $V(\mathcal{W}(\bar{x}), z_i)$, we compute six first order statistics: mean, standard deviation, skewness, kurtosis, minimum and maximum (see Appendix A.1 for formulas). Let $g : \mathbb{R}^{3 \times 3 \times 30} \rightarrow \mathbb{R}^6$ denote the feature operator. The baseline feature vector for each slice and location \bar{x} is $\mathbf{f}_{z_i}^{\text{BL}}(\bar{x}) = g(V(\mathcal{W}(\bar{x}), z_i)) \in \mathbb{R}^6$. Location wise feature vectors are mapped to bi-temporal tissue evolution masks (ROI_{RT1}^{RT2}). For each patient pt , slice z_i and bi-temporal ROI (Fig. 2), all locations in that ROI are aggregated by element-wise max pooling into a single descriptor $\mathbf{F}_{pt, \text{ROI}, z_i}^{\text{BL}} \in \mathbb{R}^6$, so each tissue-evolution class and slice is represented by one compact feature vector.

(FE2) Radiomic features capture higher order spatial texture beyond first order intensity statistics. We extract 3D gray level co-occurrence matrix (GLCM) features (Haralick et al., 1973) from $V(\bar{x}, z_i)$ using PyRadiomics (Van Griethuysen et al., 2017). For each patient pt and axial slice z_i , the volume $V(\bar{x}, z_i)$ is paired with a 3D tissue evolution mask of identical size, obtained by repeating the 2D bi-temporal ROI mask over all 30 time indexes. Symmetrical GLCMs are computed with bin width 8 and $\delta = 1$ (26 connectivity over 13 directions), yielding 24 GLCM features per slice (Fig. 3(b)). From these, we retain four descriptors: IMC1 and IMC2 (information measures of correlation 1 and 2), MCC (maximal correlation coefficient), and Correlation (formal definitions in Appendix A.2). The choice of these four features are based on the discriminative capabilities between the state-change classes observed using Mann-Whitney U tests with Bonferroni correction (Mann and

Whitney, 1947) and cliff's delta effect size(Cliff, 1993). These values for the selected four features for three tissue state-change classes are shown in Table 2 in comparison to similar statistics for baseline features. IMC1 and IMC2 quantify dependence between co-occurring gray levels, MCC reflects texture complexity, and Correlation measures linear dependence between neighbors. For each patient pt , slice z_i and bi-temporal ROI, the four values are concatenated into $\mathbf{F}_{pt, \text{ROI}, z_i}^{\text{glcm}} \in \mathbb{R}^4$, yielding one radiomic feature vector per tissue ROI and slice.

(FE3 & FE4) Deep CNN-based embeddings are capturing hierarchical, data-driven representations of ischemic tissue. We derive embeddings from two CTP segmentation encoders trained on our cohort (excluding the 18 recanalized LVO patients): (i) 2D+time mJ-Net (Tomasetti et al., 2020) that segments core and penumbra from CTP, and (ii) 2D nnU-Net (Isensee et al., 2021), also a segmentation model where each axial slice is a 512×512 image with 30 time points stacked as channels (fig. 4). In both cases, the trained networks are used in inference mode purely as feature extractors, without further fine-tuning. The CTP input for both models have gone through a preprocessing step as described in (Tomasetti et al., 2023). The 2D+time mJ-Net architecture from our previous work(Tomasetti et al., 2020) is chosen as a temporal-aware model specifically designed for core and penumbra segmentation for stroke assessment at the time of admission from CTP. Previously, we have shown that using raw CTP data and CNN based model give better results compared to using combinations of parametric maps and thresholding or classical machine learning(Tomasetti et al., 2023). For comparison, we include the 2D nn-UNet, a widely adopted, task-optimized medical image segmentation backbone that serves as a strong reference across CT and MRI applications. Our aim is not to compare predictive performance, but to assess whether features learned by CNN architectures yield interpretable tissue-evolution patterns.

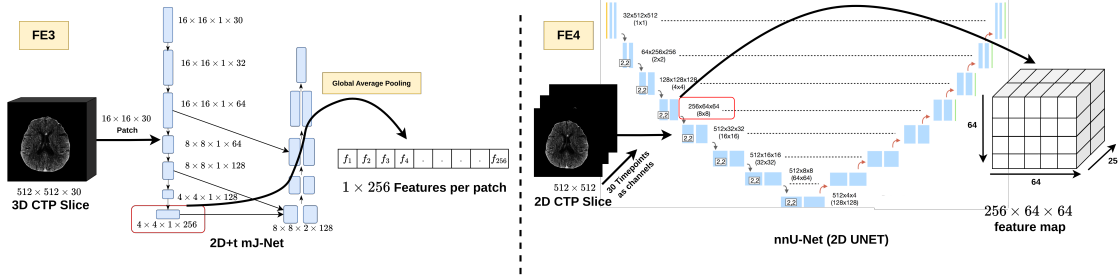


Figure 4: CNN-based deep feature extraction. Left: the 2D+time mJ-Net encoder processes $16 \times 16 \times 30$ patches and applies global average pooling on the last convolutional block to yield a 256D feature vector per patch. Right: the nnU-Net encoder produces a $256 \times 64 \times 64$ feature map, providing a 256D feature vector at each position of a downsampled 64×64 grid.

For mJ-Net, spatio-temporal patches of size $16 \times 16 \times 30$ are densely sampled over $V(\bar{x}, z_i)$ (stride 1), passed through the encoder, and activations from the last convolutional block ($4 \times 4 \times 1 \times 256$) are globally average-pooled. The resulting 256D vector is assigned to the patch centre, yielding a dense map of location-wise deep features. For each patient pt , slice z_i and bi-temporal ROI, all vectors within the ROI are aggregated by element-wise max pooling to form a slice-level mJ-Net embedding $\mathbf{F}_{pt, \text{ROI}, z_i}^{\text{mJNet}} \in \mathbb{R}^{256}$.

For nnU-Net, intermediate feature maps of size $256 \times 64 \times 64$ (channels \times height \times width) are extracted from $V(\bar{x}, z_i)$. Bi-temporal ROI masks are downsampled to 64×64 using nearest-neighbor interpolation so that each grid location inherits a tissue label. For each patient pt , slice z_i and ROI, all 256D feature vectors whose grid locations fall inside the downsampled ROI are max-pooled to obtain a slice-level nnU-Net embedding $\mathbf{F}_{pt, ROI, z_i}^{\text{nnUNet}} \in \mathbb{R}^{256}$. These embeddings act as compact CNN-based descriptors of local CTP dynamics for downstream similarity analysis, clustering and visualization (see Appendix A.3 for details).

4.1. Assessment techniques

Box plots summarize the distribution of baseline statistical and GLCM radiomic features across bi-temporal ROIs, providing a compact view of central tendency, variability and class-level overlap to qualitatively assess feature separability.

t-SNE visualization qualitatively assess the geometric structure of feature representations. The high-dimensional feature vectors were projected into two-dimensional space using t-distributed stochastic neighbor embedding (t-SNE) (Maaten and Hinton, 2008). The resulting embeddings visualize whether samples belonging to different tissue evolution ROI exhibit separable structure in feature space.

Region-wise feature discriminability is quantitatively assessed using non-parametric **statistical tests**. For each pair of bi-temporal ROIs, features are compared using Mann-Whitney U test (Mann and Whitney, 1947) due to the non-normal distribution of the data. To account for multiple feature comparisons within each region pair, Bonferroni correction (Dunn, 1961) is applied. In addition to statistical significance, effect sizes are quantified using Cliff's delta (δ) (Cliff, 1993) to assess the magnitude and direction of the distributional differences. Statistical significance is determined at $\alpha = 0.05$ after bonferroni corection (See Appendix A.4 for more details).

Cosine similarities. Similarity between CNN feature embeddings was quantified using absolute cosine similarity, defined as the absolute value of the cosine of the angle between embedding vectors. This measure captures alignment in feature space independent of vector magnitude and sign. Given two slice-level aggregated embeddings \bar{e}_i and \bar{e}_j , similarity is defined as $\text{sim}(\bar{e}_i, \bar{e}_j)$. The mean similarity between two sets of embeddings R_1 and R_2 is defined as: $\overline{\text{sim}}(R_1, R_2) = \frac{1}{|R_1||R_2|} \sum_{i \in R_1} \sum_{j \in R_2} \text{sim}(\bar{e}_i, \bar{e}_j)$.

Within- and between-group similarities were computed using slice-aggregated CNN embeddings $\mathbf{F}_{pt, ROI, z_i}^{\text{cnn}}$ for each patient, pt . A separation index, $\Delta \cos$, was defined to quantify embedding-space separation by final tissue state (infarct vs. non-infarcted brain), and is computed as the difference between average within-group similarity and between-group similarity within the same admission-defined tissue class (R is short for ROI):

$$\Delta \cos(pt) = \frac{1}{2} \left(\overline{\text{sim}}(R_1^{(pt)}, R_1^{(pt)}) + \overline{\text{sim}}(R_2^{(pt)}, R_2^{(pt)}) \right) - \overline{\text{sim}}(R_1^{(pt)}, R_2^{(pt)}), \quad (1)$$

Higher values of $\Delta \cos(pt)$ indicate stronger embedding separation by final tissue state. Statistical significance of the separation index was assessed using a one-sample Wilcoxon signed-rank test (Wilcoxon, 1945) against zero.

Additionally, slice-level vectors within an ROI are aggregated by element-wise max pooling, $\psi_{pt, ROI} = \max_{z_i} \mathbf{F}_{pt, ROI, z_i}^{\text{cnn}}$. We define $S_{pt}(ROI_1, ROI_2) = \text{sim}(\psi_{pt, ROI_1}, \psi_{pt, ROI_2})$

as *per-patient* cosine similarity and $\bar{S}(ROI_1, ROI_2) = \frac{1}{|\mathcal{P}|} \sum_{pt \in \mathcal{P}} S_{pt}(ROI_1, ROI_2)$ as *group-level* where \mathcal{P} is the set of patients for which both ROIs are present.

5. Results and discussion

The proposed framework was evaluated on 18 recanalized LVO patients. We examined 4 categories of features including BL, GLCM, and deep embeddings from mJ-Net and nnUNet across six bi-temporal ROIs defined by combining CTP and DWI labels. The CNN models were trained on all 152 patients excluding the 18 LVO patients. Figure 5 shows box plots of BL and GLCM features, where colors match ROI colors in bi-temporal mask.

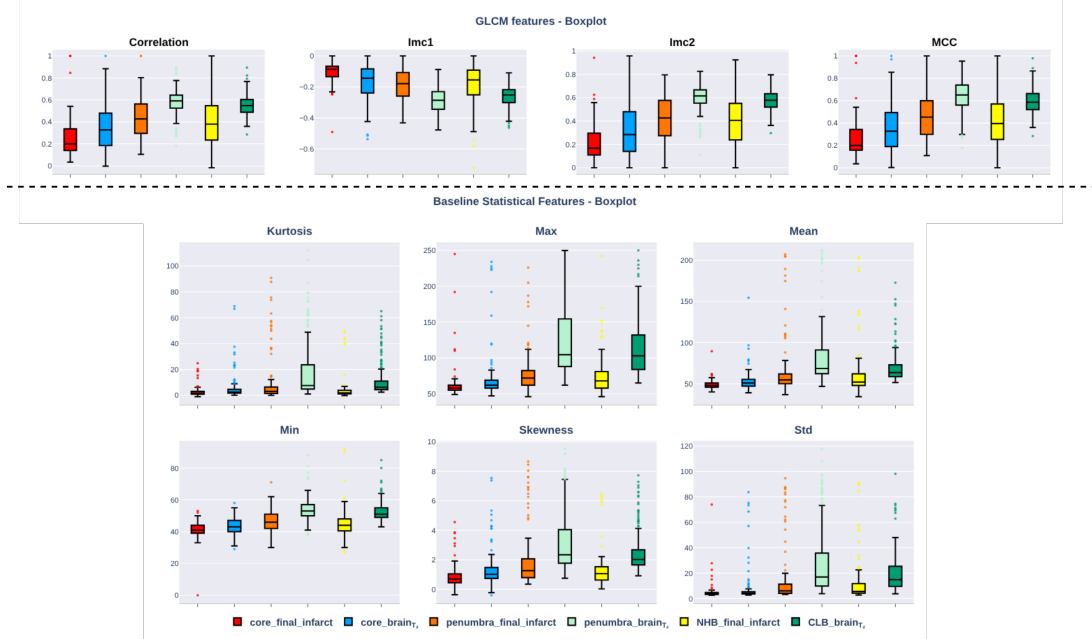


Figure 5: Box plots for GLCM and BL features over the six ROIs on slice level.

Across both GLCM and BL features a consistent trend emerges. Healthy tissue that remains viable (ROI_{CLB}^b) exhibits high median values, narrow interquartile ranges, and low variability, reflecting a stable structural phenotype. In contrast, core tissue evolving into final infarct (ROI_c^{fi}) shows lower values and greater dispersion, consistent with a disrupted or degenerating phenotype. Salvaged penumbra (ROI_p^b) generally lies between these extremes and often more closely resembles healthy tissue, suggesting a reversible phenotype. Among GLCM descriptors Imc2 provides the clearest separation between healthy/penumbra and infarcted tissue. ROI_c^{fi} and ROI_c^b display similar distributions across both GLCM and baseline features, suggesting that early core tissue at T_1 already shares textural properties with its eventual infarct outcome. Overall, while baseline intensity features show the same directional trend as GLCM, they offer weaker separation across regions, supporting the observation that texture-based metrics capture ischemic degradation more effectively than raw intensity values.

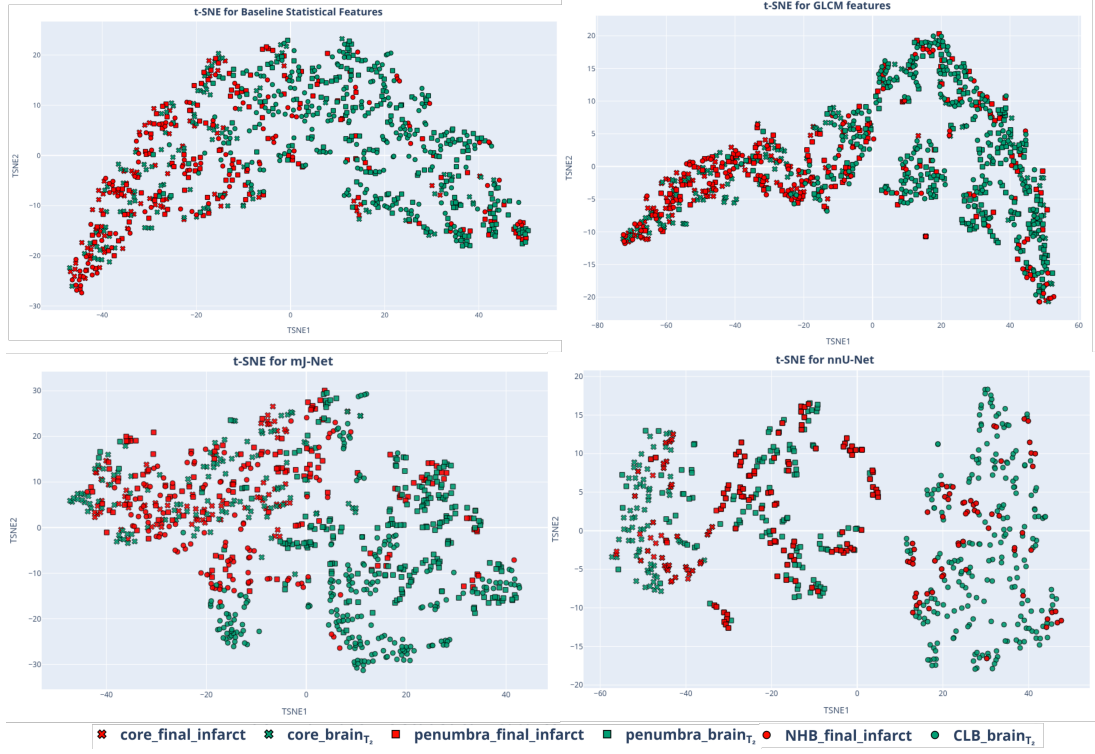


Figure 6: t-SNE of six ROI features (FE1-FE4). Symbols encode region (circle: brain; square: penumbra; cross: core); colours show $T_1 \rightarrow T_2$ tissue outcome (green: salvaged; red: infarct). Each point represents one ROI in one slice.

Figure 6 shows the t-SNE embeddings of FE1-FE4. Symbols encode anatomical regions, while colour represents tissue outcome from T_1 to T_2 . The reason for this selection is to be able to see the tissue final state better. BL and GLCM feature spaces show partial overlap between tissue types, but a visible tendency for salvaged regions (ROI_{CLB}^b , ROI_p^b , ROI_c^b) to cluster toward one side and infarct-evolving regions (ROI_{NHB}^{fi} , ROI_p^{fi} , ROI_c^{fi}) toward the other, with GLCM features forming slightly tighter clusters.

The mJ-Net, exhibits more distinct partitioning between salvaged and infarct-prone tissue among all four. The nnU-Net embedding shows an apparent gradient structure, with core tissue positioned at one extreme, healthy brain at the opposite end, and penumbra forming a transitional band between them but when it comes to distinguishing between tissue state classes it fails.

The cosine similarity values are shown in Table 1 for mJ-Net. We see high alignment for core turning either to brain (ROI_c^b) or final infarct(ROI_c^{fi}). None hypo-perfused region turning to final infarct, ROI_{NHB}^{fi} , shows high similarities to core and penumbra turning to infarct (ROI_c^{fi} , ROI_p^{fi}), 0.47, 0.41, confirming the observation in t-SNE plots.

As shown in table 2, BL and GLCM features show consistent separation between penumbra that evolves to brain or final infarct (**Test 1**), with large effect sizes and statistically significant p values. In contrast, **Test 2** shows weak separation in core region turning to

Table 1: Group-level cosine similarity for mJ-Net features, $\bar{S}(ROI1, ROI2)$

	ROI ^b _{CLB}	ROI ^{fi} _{NHB}	ROI ^b _p	ROI ^{fi} _p	ROI ^b _c	ROI ^{fi} _c
ROI ^b _{CLB}	1.00	0.36	0.46	0.3	0.26	0.22
ROI ^{fi} _{NHB}	0.36	1.00	0.44	0.47	0.41	0.47
ROI ^b _p	0.46	0.44	1.00	0.44	0.32	0.41
ROI ^{fi} _p	0.30	0.47	0.44	1.00	0.41	0.50
ROI ^b _c	0.26	0.41	0.32	0.41	1.00	0.65
ROI ^{fi} _c	0.22	0.47	0.41	0.5	0.65	1.00

Table 2: Region-pair comparisons. For baseline and GLCM: Mann–Whitney U tests with Bonferroni correction (p_{value}) and Cliff’s delta (δ) effect size (ES). For mJ-Net: Median separation index and p-values from one-sample Wilcoxon signed-rank test

Feature	Test 1: ROI_p^b vs ROI_p^{fi}			Test 2: ROI_c^b vs ROI_c^{fi}			Test 3: ROI_{NHB}^{fi} vs ROI_p^{fi}		
	p_{value}	δ	ES	p_{value}	δ	ES	p_{value}	δ	ES
Baseline statistical features									
Mean	< 0.05	0.62	L	< 0.05	0.29	S	> 0.05	-0.12	N
Std	< 0.05	0.58	L	> 0.05	0.18	S	> 0.05	0.004	N
Skewness	< 0.05	0.53	L	< 0.05	0.36	M	< 0.05	-0.21	S
Min	< 0.05	0.63	L	< 0.05	0.27	S	< 0.05	-0.20	S
Max	< 0.05	0.59	L	< 0.05	0.32	S	> 0.05	-0.10	N
Kurtosis	< 0.05	0.54	L	< 0.05	0.29	S	< 0.05	-0.24	S
GLCM features									
Imc1	< 0.05	-0.55	L	< 0.05	-0.37	M	> 0.05	0.10	N
Imc2	< 0.05	0.57	L	< 0.05	0.28	S	> 0.05	-0.08	N
Correlation	< 0.05	0.51	L	< 0.05	0.30	S	< 0.05	-0.10	N
MCC	< 0.05	0.58	L	< 0.05	0.29	S	< 0.05	-0.09	N
mJ-Net embeddings									
	Test 1: ROI_p^b vs ROI_p^{fi}			Test 2: ROI_c^b vs ROI_c^{fi}			Test 3: ROI_{NHB}^{fi} vs ROI_p^{fi}		
	p_{value}	median Δ_{cos}		p_{value}	median Δ_{cos}		p_{value}	median Δ_{cos}	
Δ_{cos}	1.5×10^{-4}	0.19		0.021	0.03		0.038	0.084	

ES: Effect Size (negligible(N)/small(S)/medium(M)/large(L)); δ : Cliff’s delta magnitude.

brain or infarct and **Test 3** shows insignificant separation between NHB and penumbra that end up as infarct. Alignment of NHB region, which was manually annotated as non-hypoperfused, with tissue evolving into final infarct, suggests that the embedded feature spaces do not fully agree with initial expert labels.

In Table 2 we also see the results of one-sample Wilcoxon signed rank test on Δ_{cos} for the same three Tests performed on deep embeddings. All tests are showing the same trend

as observed in GLCM and BL features and in t-SNE plots. Test 1 is always significant, through all types of features, pointing to a clear difference in penumbra being salvaged and penumbra ending as infarct. With this we have a stronger claim to use this analysis as an initial step towards tissue phenotyping, when validated on larger datasets.

Limitations: The limited cohort size restricts statistical power and generalizability. The study is therefore positioned as the methodological feasibility analysis, intended to evaluate the proposed feature characterization. Another limitation arises from co-registration between CTP and DWI. The two modalities differ in acquisition geometry, and CTP is frequently acquired with a head tilt to increase brain coverage under dose constraints. This introduces an axial angulation mismatch that standard 2D registration cannot fully compensate for, potentially affecting voxel-level correspondence between tissue states at T_1 and T_2 . We should note that ischemic lesions may remain unstable beyond 24-72 hours follow-up window which could affect the definition of final infarct regions and influence the interpretation of the reported results.

6. Conclusion and Future work

We presented an image-driven framework for stroke tissue characterization and used statistical, textural and deep embedding features to characterize hypoperfused regions developing to infarct vs. salvaged tissue. We observed that healthy tissue from contralateral hemisphere showed a different characteristic compared to ischemic core at admission regardless of its outcome and salvaged penumbra lies between them but more similar to CLB. None-hypoperfused at admission but infarct-evolving regions has features that are closer to core/infarct suggests that learned representations may capture latent vulnerability not apparent in initial expert labels. Clear state transition from core, penumbra to healthy tissue was seen specially in nnU-Net. Overall, our findings support the feasibility of using acute CTP-derived feature spaces as a basis for imaging phenotyping of stroke tissue evolution. While the study is limited by cohort size and reliance on a single centre, the proposed framework opens avenues for larger validation and for introducing stroke tissue phenotypes into stroke analysis. Future work will focus on extending the cohort size and we will try to evaluate our work on multicenter public datasets. Public dataset such as ISLES'24 ([Riedel et al., 2025](#)) dataset was not included in this work because they do not provide annotations or ground truth of ischemic core and penumbra at time of admission, which are required for the region level analysis performed in this work. We intend to use this dataset in our future work where we would have to rely on an automatic method to do core and penumbra segmentation.

7. Compliance with Ethical Standards

This study was conducted in accordance with institutional guidelines and approved by the regional ethical committee in Norway, and all data were pseudonymised prior to analysis.

References

Norman Cliff. Dominance statistics: Ordinal analyses to answer ordinal questions. *Psychological Bulletin*, 114(3):494–509, November 1993. ISSN 1939-1455, 0033-2909. doi: 10.1037/0033-2909.114.3.494. URL <https://doi.apa.org/doi/10.1037/0033-2909.114.3.494>.

Olive Jean Dunn. Multiple comparisons among means. *Journal of the American Statistical Association*, 56(293):52–64, 1961. doi: 10.1080/01621459.1961.10482090. URL <https://www.tandfonline.com/doi/abs/10.1080/01621459.1961.10482090>.

Robert M. Haralick, K. Sam Shanmugam, and Its'hak Dinstein. Textural features for image classification. *IEEE Trans. Syst. Man Cybern.*, 3:610–621, 1973. URL <https://api.semanticscholar.org/CorpusID:206786900>.

Fabian Isensee, Paul F Jaeger, Simon AA Kohl, Jens Petersen, and Klaus H Maier-Hein. nnu-net: a self-configuring method for deep learning-based biomedical image segmentation. *Nature methods*, 18(2):203–211, 2021.

Liang Jiang, Zhengfei Miao, Huiyou Chen, Wen Geng, Wei Yong, Yu-Chen Chen, Hong Zhang, Shaofeng Duan, Xindao Yin, and Zhiqiang Zhang. Radiomics analysis of diffusion-weighted imaging and long-term unfavorable outcomes risk for acute stroke. *Stroke*, 54(2):488–498, 2023.

Sanjukta Krishnagopal, Keith Lohse, and Robynne Braun. Stroke recovery phenotyping through network trajectory approaches and graph neural networks. *Brain Inf.*, 9(1):13, June 2022. ISSN 2198-4026. doi: 10.1186/s40708-022-00160-w. URL <https://doi.org/10.1186/s40708-022-00160-w>.

Laurens van der Maaten and Geoffrey Hinton. Visualizing data using t-sne. *Journal of machine learning research*, 9(Nov):2579–2605, 2008.

Shraddha Mainali, Marin E. Darsie, and Keaton S. Smetana. Machine learning in action: Stroke diagnosis and outcome prediction. *Frontiers in Neurology*, Volume 12 - 2021, 2021. ISSN 1664-2295. doi: 10.3389/fneur.2021.734345. URL <https://www.frontiersin.org/journals/neurology/articles/10.3389/fneur.2021.734345>.

H. B. Mann and D. R. Whitney. On a Test of Whether one of Two Random Variables is Stochastically Larger than the Other. *Ann. Math. Statist.*, 18(1):50–60, March 1947. ISSN 0003-4851. doi: 10.1214/aoms/1177730491. URL <http://projecteuclid.org/euclid.aoms/1177730491>.

Mohamed Najm, Hulin Kuang, Alyssa Federico, Uzair Jogiat, Mayank Goyal, Michael D Hill, Andrew Demchuk, Bijoy K Menon, and Wu Qiu. Automated brain extraction from head ct and cta images using convex optimization with shape propagation. *Computer Methods and Programs in Biomedicine*, 176:1–8, 2019.

Raul G Nogueira, Ashutosh P Jadhav, Diogo C Haussen, Alain Bonafe, Ronald F Budzik, Parita Bhuva, Dileep R Yavagal, Marc Ribo, Christophe Cognard, Ricardo A Hanel, et al.

Thrombectomy 6 to 24 hours after stroke with a mismatch between deficit and infarct. *New England Journal of Medicine*, 378(1):11–21, 2018.

Evamaria Olga Riedel, Ezequiel de la Rosa, The Anh Baran, Moritz Hernandez Petzsche, Hakim Baazaoui, Kaiyuan Yang, Fabio Antonio Musio, Houjing Huang, David Robben, Joaquin Oscar Seia, Roland Wiest, Mauricio Reyes, Ruisheng Su, Claus Zimmer, Tobias Boeckh-Behrens, Maria Berndt, Bjoern Menze, Daniel Rueckert, Benedikt Wiestler, Susanne Wegener, and Jan Stefan Kirschke. ISLES'24 - A Real-World Longitudinal Multimodal Stroke Dataset, November 2025. URL <https://zenodo.org/doi/10.5281/zenodo.16731717>.

S. S. Shapiro and M. B. Wilk. An analysis of variance test for normality (complete samples). *Biometrika*, 52(3-4):591–611, December 1965. ISSN 0006-3444, 1464-3510. doi: 10.1093/biomet/52.3-4.591. URL <https://academic.oup.com/biomet/article-lookup/doi/10.1093/biomet/52.3-4.591>.

Luca Tomasetti, Kjersti Engan, Mahdieh Khanmohammadi, and Kathinka Dæhli Kurz. Cnn based segmentation of infarcted regions in acute cerebral stroke patients from computed tomography perfusion imaging. In *Proceedings of the 11th ACM International Conference on Bioinformatics, Computational Biology and Health Informatics*, pages 1–8, 2020.

Luca Tomasetti, Liv Jorunn Høllesli, Kjersti Engan, Kathinka Dæhli Kurz, Martin Wilhelm Kurz, and Mahdieh Khanmohammadi. Machine Learning Algorithms Versus Thresholding to Segment Ischemic Regions in Patients With Acute Ischemic Stroke. *IEEE Journal of Biomedical and Health Informatics*, 26(2):660–672, February 2022a. ISSN 2168-2208. doi: 10.1109/JBHI.2021.3097591. URL <https://ieeexplore.ieee.org/document/9488246/?arnumber=9488246>. Conference Name: IEEE Journal of Biomedical and Health Informatics.

Luca Tomasetti, Mahdieh Khanmohammadi, Kjersti Engan, Liv Jorunn Høllesli, and Kathinka Dæhli Kurz. Multi-input segmentation of damaged brain in acute ischemic stroke patients using slow fusion with skip connection. *nldl*, 3, March 2022b. ISSN 2703-6928. doi: 10.7557/18.6223. URL <https://septentrio.uit.no/index.php/nldl/article/view/6223>.

Luca Tomasetti, Kjersti Engan, Liv Jorunn Høllesli, Kathinka Dæhli Kurz, and Mahdieh Khanmohammadi. Ct perfusion is all we need: 4d cnn segmentation of penumbra and core in patients with suspected acute ischemic stroke. *IEEE Access*, 11:138936–138953, 2023. ISSN 2169-3536.

Anh T Tran, Junhao Wen, Gaby Abou Karam, Dorin Zeevi, Adnan I Qureshi, Ajay Malhotra, Shahram Majidi, Niloufar Valizadeh, Santosh B Murthy, Mert R Sabuncu, et al. Comparing handcrafted radiomics versus latent deep learning features of admission head ct for hemorrhagic stroke outcome prediction. *BioTech*, 14(4):87, 2025.

Joost JM Van Griethuysen, Andriy Fedorov, Chintan Parmar, Ahmed Hosny, Nicole Aucoin, Vivek Narayan, Regina GH Beets-Tan, Jean-Christophe Fillion-Robin, Steve Pieper, and Hugo JW Aerts. Computational radiomics system to decode the radiographic phenotype. *Cancer research*, 77(21):e104–e107, 2017.

Janita E Van Timmeren, Davide Cester, Stephanie Tanadini-Lang, Hatem Alkadhi, and Bettina Baessler. Radiomics in medical imaging—“how-to” guide and critical reflection. *Insights into imaging*, 11(1):91, 2020.

Freda Werdiger, Mark W. Parsons, Milanka Visser, Christopher Levi, Neil Spratt, Tim Kleinig, Longting Lin, and Andrew Bivard. Machine learning segmentation of core and penumbra from acute stroke ct perfusion data. *Frontiers in Neurology*, Volume 14 - 2023, 2023. ISSN 1664-2295. doi: 10.3389/fneur.2023.1098562. URL <https://www.frontiersin.org/journals/neurology/articles/10.3389/fneur.2023.1098562>.

Frank Wilcoxon. Individual Comparisons by Ranking Methods. *Biometrics Bulletin*, 1(6): 80, December 1945. ISSN 00994987. doi: 10.2307/3001968. URL <https://www.jstor.org/stable/10.2307/3001968?origin=crossref>.

Max Wintermark, Adam E. Flanders, Birgitta Velthuis, Reto Meuli, Maarten van Leeuwen, Dorit Goldsher, Carissa Pineda, Joaquin Serena, Irene van der Schaaf, Annet Waaijer, James Anderson, Gary Nesbit, Igal Gabriely, Victoria Medina, Ana Quiles, Scott Pohlman, Marcel Quist, Pierre Schnyder, Julien Bogousslavsky, William P. Dillon, and Salvador Pedraza. Perfusion-ct assessment of infarct core and penumbra. *Stroke*, 37 (4):979–985, 2006. doi: 10.1161/01.STR.0000209238.61459.39. URL <https://www.ahajournals.org/doi/abs/10.1161/01.STR.0000209238.61459.39>.

Ona Wu, Stefan Winzeck, Anne-Katrin Giese, Brandon L. Hancock, Mark R. Etherton, Mark J.R.J. Bouts, Kathleen Donahue, Markus D. Schirmer, Robert E. Irie, Steven J.T. Mocking, Elissa C. McIntosh, Raquel Bezerra, Konstantinos Kamnitsas, Petrea Frid, Johan Wasselius, John W. Cole, Huichun Xu, Lukas Holmegaard, Jordi Jiménez-Conde, Robin Lemmens, Eric Lorentzen, Patrick F. McArdle, James F. Meschia, Jaume Roquer, Tatjana Rundek, Ralph L. Sacco, Reinhold Schmidt, Pankaj Sharma, Agnieszka Slowik, Tara M. Stanne, Vincent Thijs, Achala Vagal, Daniel Woo, Stephen Bevan, Steven J. Kittner, Braxton D. Mitchell, Jonathan Rosand, Bradford B. Worrall, Christina Jern, Arne G. Lindgren, Jane Maguire, Natalia S. Rost, on behalf of the MRI-GENIE, and GISCOME Investigators. Big data approaches to phenotyping acute ischemic stroke using automated lesion segmentation of multi-center magnetic resonance imaging data. *Stroke*, 50(7):1734–1741, 2019. doi: 10.1161/STROKEAHA.119.025373. URL <https://www.ahajournals.org/doi/abs/10.1161/STROKEAHA.119.025373>.

Wenjin Yang, Jan W. Hoving, Miou S. Koopman, Manon L. Tolhuisen, Henk van Voorst, Olvert A. Berkhemer, Jonathan M. Coutinho, Ludo F. M. Been, and Bart J. Emmer. Agreement between estimated computed tomography perfusion ischemic core and follow-up infarct on diffusion-weighted imaging. *Insights into Imaging*, 13(1):191, December 2022. ISSN 1869-4101. doi: 10.1186/s13244-022-01334-0. URL <https://doi.org/10.1186/s13244-022-01334-0>.

Appendix A. Supplementary Materials

A.1. FE1: Baseline (BL) statistical features

We provide the formulas for the baseline statistical features used in Sec. 4. Consider the sliding window $\mathcal{W}(\bar{x}) \in \mathbb{R}^{3 \times 3 \times 30}$ denote the local spatio-temporal window centred at \bar{x} as defined in Sec. 4. The intensities in $V(\mathcal{W}(\bar{x}), z_i)$ are collected into a vector $\{\zeta_j\}_{j=1}^N$ with $N = 3 \times 3 \times 30 = 270$.

$$\begin{aligned}\mu(\bar{x}) &= \frac{1}{N} \sum_{j=1}^N \zeta_j & \sigma(\bar{x}) &= \sqrt{\frac{1}{N} \sum_{j=1}^N (\zeta_j - \mu(\bar{x}))^2} \\ \text{skew}(\bar{x}) &= \frac{1}{N} \sum_{j=1}^N \left(\frac{\zeta_j - \mu(\bar{x})}{\sigma(\bar{x})} \right)^3 & \text{kurt}(\bar{x}) &= \frac{1}{N} \sum_{j=1}^N \left(\frac{\zeta_j - \mu(\bar{x})}{\sigma(\bar{x})} \right)^4 - 3 \\ v_{\min}(\bar{x}) &= \min_{1 \leq j \leq N} \zeta_j & v_{\max}(\bar{x}) &= \max_{1 \leq j \leq N} \zeta_j\end{aligned}$$

Here $\mu(\bar{x})$ and $\sigma(\bar{x})$ denote the local mean and standard deviation, $\text{skew}(\bar{x})$ and $\text{kurt}(\bar{x})$ are the skewness and kurtosis of the local intensity distribution, and $v_{\min}(\bar{x})$, $v_{\max}(\bar{x})$ are the minimum and maximum attenuation values within $\mathcal{W}(\bar{x})$. The “ -3 ” in $\text{kurt}(\bar{x})$ sets the kurtosis of a normal distribution to zero for easier interpretation.

Let $g : \mathbb{R}^{3 \times 3 \times 30} \rightarrow \mathbb{R}^6$ denote the baseline feature operator that maps a window $\mathcal{W}(\bar{x})$ to the six statistics above. The baseline feature vector at slice z_i and location \bar{x} is then

$$\mathbf{f}_{z_i}^{\text{BL}}(\bar{x}) = g(\mathcal{W}(\bar{x})) = [\mu(\bar{x}), \sigma(\bar{x}), \text{skew}(\bar{x}), \text{kurt}(\bar{x}), v_{\min}(\bar{x}), v_{\max}(\bar{x})]^\top \in \mathbb{R}^6.$$

For each patient pt , slice z_i and bi-temporal region of interest ROI, we define the slice-level baseline descriptor by element-wise max pooling,

$$\mathbf{F}_{pt, \text{ROI}, z_i}^{\text{BL}} = \max_{\bar{x} \in \text{ROI}_{pt, z_i}} \mathbf{f}_{z_i}^{\text{BL}}(\bar{x}) \in \mathbb{R}^6,$$

where ROI_{pt, z_i} denotes the set of locations \bar{x} on slice z_i assigned to that bi-temporal tissue-evolution class.

A.2. FE2: Radiomic features

This appendix gives the formal definitions (Haralick et al., 1973) of the four GLCM-based radiomic descriptors used in Sec. 4. All notation and preprocessing (3D GLCMs computed from $V(\bar{x}, z_i)$ and the corresponding 3D tissue-evolution masks, bin width 8, $\delta = 1$, 26-connectivity) follow Sec. 4.

Let ϵ be an arbitrary small positive number, $p(i, j)$ denote the normalized gray-level co-occurrence matrix (GLCM) for a fixed distance/orientation pair, and let N_g be the number of gray levels. The marginal distributions are

$$p_x(i) = \sum_{j=1}^{N_g} p(i, j), \quad p_y(j) = \sum_{i=1}^{N_g} p(i, j),$$

with means μ_x, μ_y and standard deviations σ_x, σ_y . The entropies of p_x , p_y and $p(i, j)$ are

$$\begin{aligned} HX &= - \sum_{i=1}^{N_g} p_x(i) \log_2(p_x(i) + \epsilon), & HY &= - \sum_{j=1}^{N_g} p_y(j) \log_2(p_y(j) + \epsilon), \\ HXY &= - \sum_{i=1}^{N_g} \sum_{j=1}^{N_g} p(i, j) \log_2(p(i, j) + \epsilon). \end{aligned}$$

The Haralick cross-entropy terms are

$$\begin{aligned} HXY1 &= - \sum_{i=1}^{N_g} \sum_{j=1}^{N_g} p(i, j) \log_2(p_x(i)p_y(j) + \epsilon), \\ HXY2 &= - \sum_{i=1}^{N_g} \sum_{j=1}^{N_g} p_x(i)p_y(j) \log_2(p_x(i)p_y(j) + \epsilon). \end{aligned}$$

Using these quantities, the four radiomic descriptors are defined as

$$\begin{aligned} \text{Imc1} &= \frac{HXY - HXY1}{\max\{HX, HY\}}, & \text{Imc2} &= \sqrt{1 - \exp(-2(HXY2 - HXY))}, \\ \text{MCC} &= \sqrt{\lambda_2(Q)}, & \text{corr} &= \frac{\sum_{i,j=1}^{N_g} i j p(i, j) - \mu_x \mu_y}{\sigma_x \sigma_y}, \end{aligned}$$

where $\lambda_2(Q)$ is the second-largest eigenvalue of

$$Q(i, j) = \sum_{k=1}^{N_g} \frac{p(i, k)p(j, k)}{p_x(i)p_y(k)}.$$

IMC1 and IMC2 quantify the statistical dependence between co-occurring gray levels (IMC1 in $[-1, 0]$, IMC2 in $[0, 1]$), MCC measures texture complexity (typically in $[0, 1]$), and corr captures the linear dependence of neighbouring gray levels. For each patient pt , slice z_i and bi-temporal ROI, these four quantities are computed on the corresponding 3D tissue-evolution mask and concatenated into the radiomic feature vector

$$\mathbf{F}_{pt, \text{ROI}, z_i}^{\text{glcm}} = [\text{Imc1}, \text{Imc2}, \text{MCC}, \text{corr}] \in \mathbb{R}^4,$$

A.3. FE3 & FE4

(FE3 & FE4) Deep CNN-based embeddings provide slice-wise representations derived from two pretrained CTP segmentation encoders: a 2D + time mJ-Net variant and a 2D nnU-Net (see main text and Fig. 4). In both cases, the networks are used in inference mode as frozen feature extractors; no additional fine-tuning is applied when generating embeddings.

mJ-Net encoder (FE3). From each 3D CTP slice $V(\bar{x}, z_i)$, we extract spatio-temporal patches $16 \times 16 \times 30$ on a dense grid with unit in-plane stride. We use last encoder block to get features of size $4 \times 4 \times 1 \times 256$. Global average pooling over the spatial and depth axes yields a 256-dimensional descriptor, which we associate with the central in-plane location, giving a dense map of location-wise features $\mathbf{f}_{z_i}^{\text{mJNet}}(\bar{x}) \in \mathbb{R}^{256}$. These maps are aligned with the bi-temporal tissue-evolution masks. For each patient pt , slice z_i and ROI, all $\mathbf{f}_{z_i}^{\text{mJNet}}(\bar{x})$ whose locations fall inside the corresponding region are aggregated by element-wise max pooling,

$$\mathbf{F}_{pt, \text{ROI}, z_i}^{\text{mJNet}} = \max_{\bar{x} \in \text{ROI}_{pt, z_i}} \mathbf{f}_{z_i}^{\text{mJNet}}(\bar{x}) \in \mathbb{R}^{256},$$

yielding one 256D mJ-Net embedding per slice and tissue-evolution class.

nnU-Net encoder (FE4). For the nnU-Net backbone, we extract intermediate encoder feature maps of size $256 \times 64 \times 64$ (channels \times height \times width) for each slice z_i . Let $\mathbf{f}_{z_i}^{\text{nnUNet}}(u, v) \in \mathbb{R}^{256}$ denote the feature vector at grid location (u, v) in this 64×64 map. The bi-temporal ROI masks defined at 512×512 resolution are downsampled to 64×64 using nearest-neighbour interpolation so that each (u, v) inherits a unique tissue label. For each patient pt , slice z_i and ROI, the nnU-Net features whose grid locations lie within the downsampled region are aggregated by element-wise max pooling,

$$\mathbf{F}_{pt, \text{ROI}, z_i}^{\text{nnUNet}} = \max_{(u, v) \in \text{ROI}_{pt, z_i}^{64 \times 64}} \mathbf{f}_{z_i}^{\text{nnUNet}}(u, v) \in \mathbb{R}^{256}.$$

Thus, both mJ-Net (FE3) and nnU-Net (FE4) provide one compact 256D deep embedding per patient, slice and bi-temporal ROI, which is used for similarity analysis, clustering and visualization in the main experiments.

A.4. Statistical Tests

Statistical analysis was performed on slice-level baseline statistical features and GLCM texture features extracted for each patient pt , slice z_i and bi-temporal ROIs. Let, $x_{pt, \text{ROI}, z_i}^{(k)} \in \mathbb{R}$ denote the value of feature k associated with patient pt , slice z_i and ROI where k indexes baseline statistical feature or GLCM feature descriptor.

For each feature k , the distribution of values across ROI categories is first assessed for normality using Shapiro-Wilk test (Shapiro and Wilk, 1965). As the null hypothesis normality is rejected for the majority of the features ($p < 0.05$), subsequent analyses is relied on non-parametric statistical testing.

Pairwise comparisons between ROI categories are conducted using the Mann-Whitney U test (Mann and Whitney, 1947) applied to the corresponding sets of feature values $x_{pt, \text{ROI}_a, z_i}^{(k)}$ and $x_{pt, \text{ROI}_b, z_i}^{(k)}$. Statistical significance is evaluated using two-sided tests with a significance level of $\alpha = 0.05$. To account for multiple pairwise comparisons across ROI categories, Bonferroni correction (Dunn, 1961) is applied to all p values.

In addition to statistical significance testing, effect sizes of two ROIs is quantified using cliff's delta (δ) (Cliff, 1993). Effect sizes are interpreted using the standard thresholds,

$$\begin{aligned} |\delta| < 0.147 & \text{ (negligible),} & 0.147 \leq |\delta| < 0.33 & \text{ (small),} \\ 0.33 \leq |\delta| < 0.474 & \text{ (medium),} & |\delta| \geq 0.474 & \text{ (large).} \end{aligned}$$

Given the limited cohort size, both corrected p values and effect sizes are reported to characterize differences in baseline and texture features while avoiding over-reliance on statistical significance alone.